Available online at www.sciencedirect.com
SCIENCE DIRECT®
Journal of Power Sources 136 (2004) 72–79
JOURNAL OF POWER SOURCES
www.elsevier.com/locate/jpowsour

Structural studies of $Li_{4/3}Me_{5/3}O_4$ (Me = Ti, Mn) electrode materials: local structure and electrochemical aspects

C.M. Julien [a], M. Massot [b], K. Zaghib [c,*]

[a] *Laboratoire des Milieux Désordonnés et Hétérogènes, CNRS-UMR 7603, Université Pierre et Marie Curie, 140 rue de Lourmel, 75015 Paris, France*
[b] *Laboratoire de Physique de la Matière Condensée, CNRS-UMR 7602, Université Pierre et Marie Curie, 4 Place Jussieu, Case 77, 75252 Paris cedex 05, France*
[c] *Institut de Recherche d'Hydro-Québec (IREQ), 1800 Boul, Lionel-Boulet, Varennes, Que., Canada J3X 1S1*

Received 5 April 2004; accepted 1 May 2004

Available online 28 July 2004

Abstract

Raman scattering spectroscopy have been applied to the study of local structure of $Li_{4/3}Me_{5/3}O_4$ (Me = Ti, Mn) spinel oxides used as electrode materials for rechargeable lithium batteries and hybrid supercapacitors. We report the analysis of their vibrational spectra using both the classical factor group analysis and a local environment model. Electrochemical performance was carried out using a lithium cell with solvent-free solid-polymer. Raman spectra of $Li_{4/3+x}Me_{5/3}O_4$ spinels are compared and analyzed on the basis of structural modifications of their lattices upon lithium insertion.

Keywords: Spinel; Lattice dynamics; Raman spectroscopy; Lithium batteries

1. Introduction

Recently, lithium titanium oxide spinels are becoming the promising negative electrode materials in terms of the intercalation potential, cyclability and rate capability for the development of polymer (or ceramic) lithium-ion batteries and hybrid supercapacitors [1–4]. The $[Me_2]O_4$ framework of an $Li[Me_2]O_4$ spinel is an attractive host structure for lithium insertion–extraction reactions because it provides a three-dimensional network of face-sharing tetrahedra and octahedra for lithium ion diffusion. The zero-strain insertion material $Li_{4/3}Ti_{5/3}O_4$ ($Li_4Ti_5O_{12}$) was intensively studied because it exhibits the best behavior and reversibly inserts 0.7–1.0 Li per mole of oxide at 1.55 V leading to a specific capacity of 150 mAh/g (against a theoretical capacity of 175 mAh/g) [3–10]. The exceptional stability of this electrode to electrochemical cycling has been demonstrated by Rossen et al. [6] and can be attributed to the stability of the $[Ti_{1.67}Li_{0.33}]O_4$ framework and to the minimal dilation (<1%) of the cubic unit cell that occurs on lithium insertion. The demonstration of the use of $Li_4Ti_5O_{12}$ as a negative electrode in a high-power lithium battery with safety concern has been done. Excellent cycle life was achieved for $Li_4Ti_5O_{12}$//$LiCoO_2$ cells, as is expected with lithium intercalation–deintercalation into stable metal oxide structures [11].

Lithium titanate $Li_{1+z}Ti_{2-z}O_4$ are rather complex materials and show a homogeneity range for $0 \leq z \leq 0.33$ that enables it to exhibit a varied fundamental properties. $LiTi_2O_4$ is a dark-blue metallic compound whereas the end-member $Li_{4/3}Ti_{5/3}O_4$ is white and insulating. According to previous studies [5–8], the spinel phase $LiTi_2O_4$ consists of a close-packed array, in which oxygen atoms occupy 32e sites of space group $Fd3m$, octahedral 16d sites and tetrahedral 8a sites are fully occupied by metal ions (here titanium) and lithium. In the case of $Li_{4/3}Ti_{5/3}O_4$ which has a higher Li/Ti ratio (0.8) than $LiTi_2O_4$ (0.5), substitution of titanium by lithium ions occurs in octahedral sites. Ohzuku et al. [8] have suggested the following formula $Li^{8a}[Li_{1/3}Ti_{5/3}]^{16d}O_4$. According to Bach et al. [10] the structure of $Li_{4+x}Ti_5O_{12}$ is practically unchanged as Li accommodation proceeds since the typical diffraction pattern of the parent oxide is recovered, even at a high depth of discharge. For instance, at $x = 0.9$, the spinel structure is maintained with only a

* Corresponding author. Tel.: +1 450 652 8019; fax: +1 450 652 8424.
E-mail address: zaghib.karim@ireq.ca (K. Zaghib).

0378-7753/$ – see front matter © 2004 Elsevier B.V. All rights reserved.
doi:10.1016/j.jpowsour.2004.05.001

negligible modification in the cubic lattice parameter from 8.344 to 8.357 Å. These results have been evidenced using high-angle X-ray scans, which show the ordered rock-salt structure of lithiated $Li_{2.33}Ti_{1.67}O_4$ spinel [12].

Experimentally, as far as we know, only Raman measurements have been reported by Liu et al. [13], whereas theoretically the lattice dynamics of the spinel phases $Li_{1+z}Ti_{2-z}O_4$ have been made by Sinha and Gupta [14]. However, the literature is very scarce with data concerning vibrational spectra of defect spinels [15].

This work reports on the structural characterization of $Li_4Ti_5O_{12}$ spinel lattice by X-ray powder diffractometry (XRPD), and scanning electron microscopy (SEM). Because the structural determination is an important point and XRPD is not the most suitable technique for studying structural effects related to light atoms, such as lithium, a spectroscopic study, i.e. Raman scattering (RS), was performed to confirm the proposed structural model. The lattice modes of the $Li_4Ti_5O_{12}$ and $Li_4Mn_5O_{12}$ spinels are discussed in the spectroscopic symmetry, and the vibrations due to lithium ions with their oxygen neighbors are identified. The electrochemical features of $Li_4Ti_5O_{12}$ nanostructured powders have been studied by coupling them in gel–electrolyte lithium cells. Raman spectra of $Li_{4+x}Me_5O_{12}$ lithium inserted frameworks are compared with pristine materials, and analyzed on the basis of structural modifications of their lattices upon lithium insertion.

2. Experimental

The $Li_4Ti_5O_{12}$ powder samples were synthesized by high-energy ball milling (HEBM) of precursor to form nanocrystalline phases. Samples were then heat treated to obtain the impurity-free $Li_4Ti_5O_{12}$ nanophases. The prepared samples of Li–Ti–O ternary phases were white in color. The $Li_{4/3}Mn_{5/3}O_4$ powders were prepared using a wet-chemical ('chimie douce') method assisted by succinic acid as described elsewhere [16].

The crystal structure of $Li_4Ti_5O_{12}$ samples was characterized by X-ray powder diffraction (XRPD) using a diffractometer (Philips model PW1830) with nickel-filtered Cu Kα radiation ($\lambda = 1.5406$ Å). The diffraction patterns were taken at room temperature in the range of $5^\circ < 2\theta < 80^\circ$ using step scans. The morphologies of the sample particles were examined by scanning electron microscopy using a Hitachi S-570 apparatus.

Raman spectra of lithium-containing samples were recorded on a Jobin-Yvon U1000 double monochromator equipped with a spatial filter. The 514.5 nm line from a Spectra-Physics 2020 argon-ion laser was used as excitation source. Standard photon-counting techniques were used for detection. In a typical spectral acquisition, six RS spectra each recorded with a resolution of $2\,cm^{-1}$ were averaged to increase the signal-to-noise ratio. To avoid sample photo-decomposition or denaturation, RS spectra were recorded using a low excitation power of 10 mW.

The discharge–charge cycle for the electrode was made in lithium cells with gel electrolyte. Measurements were carried out using a Macpile potentiostat in the galvanostatic mode in the potential range 2.5–1.2 V at current density 7.23 mA/g (*C*/12 rate). The lithium anode was used as reference electrode by pressing the lithium foil on stainless steel disk. The gel electrolyte consisted of SPE:copolymer based on POE and LiTFSI (1.5 M) salt (EC + YBL + TESA in the ratio 1:2:1).

3. Results and discussion

3.1. Structure and morphology

Fig. 1a and b shows the X-ray diffraction diagrams of $Li_{4/3}Me_{5/3}O_4$ obtained for Ti and Mn sample. The XRPD patterns of HEBM synthesized $Li_{4/3}Ti_{5/3}O_4$ show a single phase that is an impurity-free material where the presence of TiO_2 (anatase) is not detected (Fig. 1a). For $Li_{4/3}Mn_{5/3}O_4$ sample synthesized by wet chemistry, the Bragg lines correspond to that single-phase with a high crystallinity (Fig. 1b). The crystal structure of $Li_{4/3}Me_{5/3}O_4$ was analyzed assuming a defect spinel framework and the diffraction lines were indexed in terms of cubic space group. The lattice parameters were evaluated by a method using 12 diffraction lines. Structural parameter of $Li_{4/3}Ti_{5/3}O_4$ was calculated to be $a = 8.365(2)$ Å. This value is consistent with that reported for $Li_{4/3}Ti_{5/3}O_4$ [4–8]. The lattice parameter of $Li_{4/3}Mn_{5/3}O_4$ was found to be $a = 8.161(1)$ Å. The XRD patterns of $Li_{4/3}Mn_{5/3}O_4$ are also consistent with the spinel structure. A detailed study of the preparation shows that samples heated at 450 °C for 10 h have good crystallinity without unwanted extra phases. However, minor impurities such as Mn_3O_4

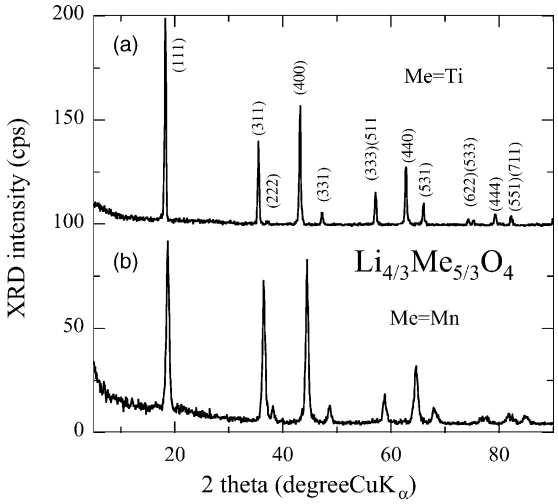

Fig. 1. X-ray powder diffraction diagrams of $Li_{4/3}Mn_{5/3}O_4$ spinels (Me = Ti, Mn).

and Li_2MnO_3 appeared when the reaction temperature was raised above 600 °C.

The crystallographic structure of $Li_{4/3}Ti_{5/3}O_4$ was reported by Ohzuku et al. [8]. Zaghib et al. [3] have analyzed its stability by X-ray diffraction and in-situ scanning electron microscopy and demonstrated that $Li_{4/3}Ti_{5/3}O_4$ is a zero-strain insertion material that offers advantages for the solid-polymer electrolyte cell including safety, long life, and reliability. It is assumed that, in the cubic structure of $Li_{4/3}Ti_{5/3}O_4$, lithium ions are located at the tetrahedral 8a (Wyckoff notation) sites, and tetravalent titanium ions ($3d^0$) and lithium ions are randomly distributed at octahedral 16d sites by the ratio Li/Ti = 1/5, while oxygen ions are located at the 32e sites with the oxygen positional parameter, $u = 0.265$. Thus, in the spinel notation, the formula of lithium titanate is $Li^{8a}[Li_{1/3}Ti_{5/3}]^{16d}$.

Surface morphology and texture as well as particle sizes of $Li_{4/3}Me_{5/3}O_4$ samples were observed by scanning electron microscopy. Fig. 2(a–d) shows typical SEM pictures of $Li_{4/3}Ti_{5/3}O_4$ spinel synthesized by the HEBM method. It can be seen that the narrow particles in the sample are highly regular. Either size or the form of the particles is even. It can be explained by the high crystallinity and the absence of defects in the crystallites. Most of the particles have regular shape with roundness of the edges, and their dimensions are submicron-sized, i.e. the grain size average is around 600 nm. The SEM micrographs of $Li_{4/3}Ti_{5/3}O_4$ show a rather homogeneous size distribution of the nanoparticles. The marked decrease in the particle size of $Li_{4/3}Ti_{5/3}O_4$ spinels is then unequivocally correlated with kinetics of grain formation using the proposed HEBM synthesis which favors the tendency of small grains. Since electrochemical lithium intercalation and deintercalation are in general limited by the rate of diffusion, the aforementioned features are important since smaller grain size can favor the lithium-ion mobility in the particles by reducing the ion-diffusion pathway. The specific surface area of $Li_{4/3}Ti_{5/3}O_4$ was measured by BET method (Nova 2000) and found to be 2.74 m^2/g.

Similar morphology is shown for $Li_{4/3}Mn_{5/3}O_4$ samples synthesized by wet chemistry. The typical SEM image of $Li_{4/3}Mn_{5/3}O_4$ shown in Fig. 3a and b clearly displays the regular shape of the crystallites. They are uniformly distributed between 0.4 and 0.9 μm. Such uniformity in size

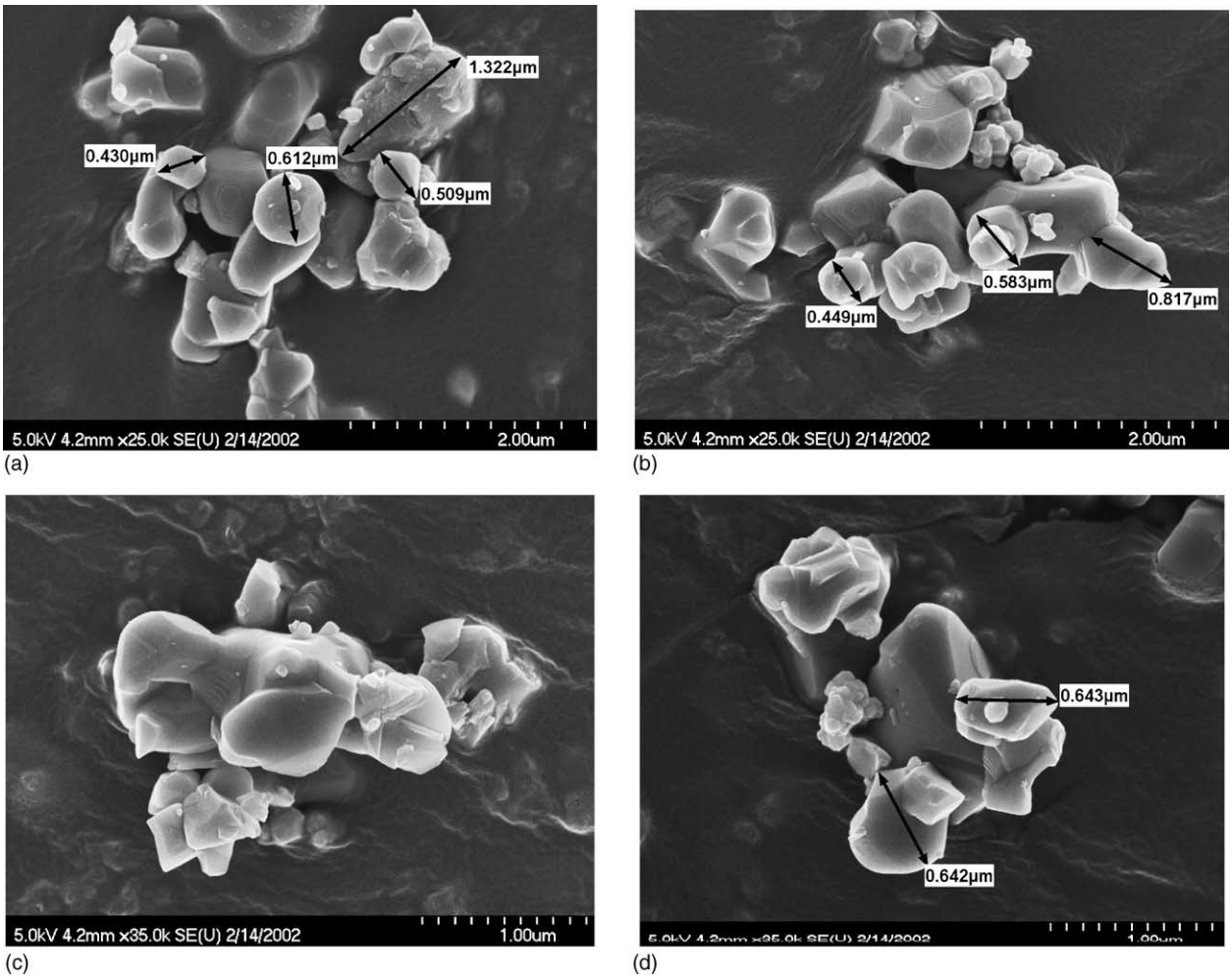

Fig. 2. SEM pictures of nanostructured $Li_{4/3}Ti_{5/3}O_4$ powders synthesized by HEBM.

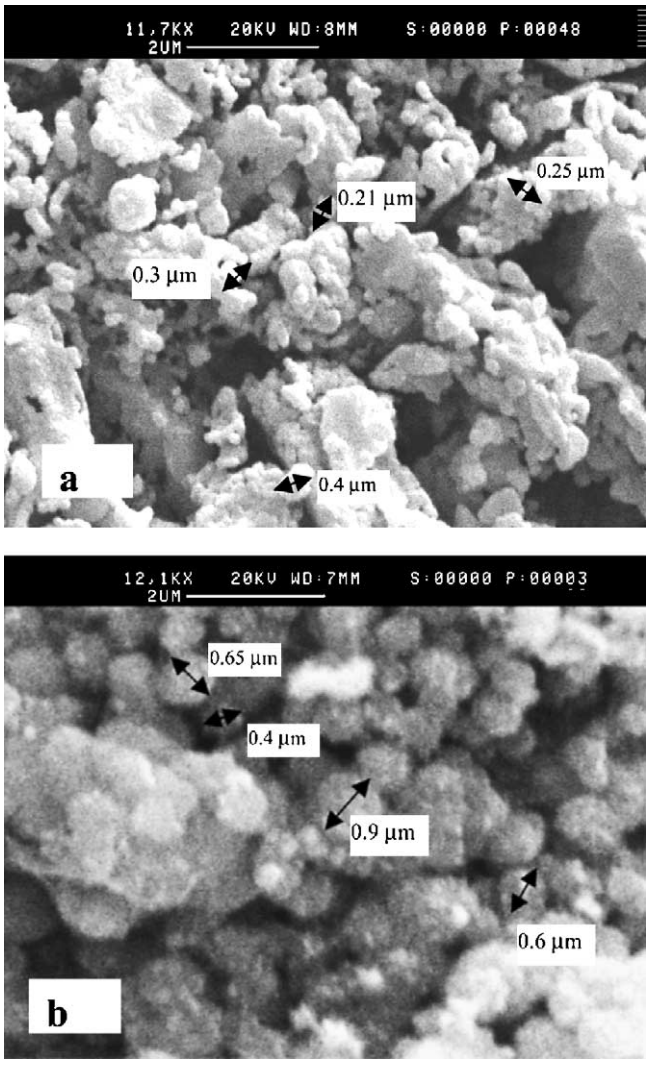

Fig. 3. SEM pictures of nanostructured $Li_{4/3}Mn_{5/3}O_4$ powders synthesized by wet chemistry.

and shape of the particles could be the result of the homogeneity of the Li–Mn–O succinate precursor.

3.2. Vibrational spectroscopy

Analysis of the vibrational spectra of $A[B]_2O_4$ spinel oxides can be made by the classical factor group theory using spectroscopic symmetry; but it is also convenient to analyze Raman and infrared spectra in terms of localized vibrations, considering the $LiTi_2O_4$ spinel structure constituted by TiO_6 octahedral and LiO_4 tetrahedral units, which can be considered as weakly connected.

In the $A[B]_2O_4$ spinel structure some of the differences between a factor group and the isomorphous point group become more in evidence. The case in point is the class of the horizontal mirror planes, σ_h. The tetrahedral A atoms lie on the σ_h planes and according to the point group operation would remain invariant under this operation and thus contribute to the character. In the factor group σ_h is a glide plane, the atoms do not remain invariant and thus do not contribute to the character. The corresponding site symmetry for the spectroscopic symmetry which contains both the infrared and Raman active modes is given by

$$2T_d(8),\ 2D_{3d}(16),\ C_{3v}(32),\ C_{2v}(48),\ C_s(96),\ C_2(96),\ C_1(192) \quad (1)$$

where each site-group symbol is preceded by an integer indicating the number of distinct sites of each symmetry and followed by the multiplicity in parentheses. As pointed out by White and De Angelis [17], the full cubic cell of spinel is redundant since only the two octants of the cell which lie along the main body diagonal are really different. The full cell contains 56 atoms, the reduced cell (equivalent to the rhombohedral smallest Bravais cell) contains only 14 atoms. Thus, in the counting procedure four times as many atoms were counted as were necessary. The reducible representation can thus be devised by four and still contains all the non-redundant information. Using the characters of the reducible representation and the character table for point group O_h, the symmetries and selection rules for the normal modes of $A[B_2]O_4$ spinel were calculated [18].

Factor-group theoretical treatment of normal $A[B_2]O_4$ spinel-type compounds yields nine optic modes allowed at the centre of the Brillouin zone ($\vec{q} = \vec{0}$). The total irreducible representation for the vibrational modes of $Li_4Mn_5O_{12}$ is obtained (Table 1) as

$$\Gamma = A_{1g} \oplus E_g + F_{1g} \oplus 3F_{2g} \oplus 2A_{2u} \oplus 2E_u \oplus 6F_{1u} \oplus 2F_{2u} \quad (2)$$

in which five optic modes are zone-centre Raman-active vibrations ($A_{1g} \oplus E_g \oplus 3F_{2g}$) and six are infrared-active vibrations ($6F_{1u}$). The remaining ($F_{1g} \oplus 2A_{2u} \oplus 2E_u \oplus 2F_{2u}$) are inactive modes [17,18]. It is interesting to note that the factor-group analysis of $Li_4Mn_5O_{12}$ is slightly different than that of $LiMn_2O_4$ due to the presence of Li ions in both tetrahedral (T_d site symmetry) and octahedral (D_{3d} site symmetry) positions participate in the F_{1u} infrared-active modes, while the tetrahedrally coordinated Li ions only participate in the F_{2g} Raman mode. Additional infrared bands are expected because the simultaneous occupation of the octahedral positions by Li and Ti, two ions with different mass and charge.

Fig. 4 shows the RS spectra of $Li_{4/3}Ti_{5/3}O_4$ and $Li_4Mn_5O_{12}$ microcrystalline samples in the region between 100 and 900 cm^{-1}. These spectra show common features; as observed in spinel oxides and in other manganese oxides, energies of ~600–650 cm^{-1} are characteristic of vibrations involving motion of oxygen atoms inside the octahedral unit MeO_6 (Me = Mn, Ti). Less intense spectroscopic structures are detectable below 500 cm^{-1} in each sample. We point out that, among the five predicted Raman modes, a higher number of peaks is observed for $Li_{4/3}Ti_{5/3}O_4$ and $Li_{4/3}Mn_{5/3}O_4$ as well. A detailed analysis of the spectra

Table 1
Factor group analysis of the $Li_4Ti_5O_{12}$ spinel structure (space group)

Atom	Site	Irreducible representation
Li_{tetra}	T_d	$F_{2g} \oplus F_{1u}$
Li_{octa}	D_{3d}	$2F_{1u} \oplus A_{2u} \oplus E_u \oplus F_{2u}$
Ti	D_{3d}	$2F_{1u} \oplus A_{2u} \oplus E_u \oplus F_{2u}$
O	C_{2v}	$A_{1g} \oplus E_g \oplus 2F_{2g} \oplus 2F_{1u} \oplus F_{1g} \oplus A_{2u} \oplus E_u \oplus F_{2u}$
Total	$A_{1g} \oplus E_g \oplus 3F_{2g} \oplus 7F_{1u} \oplus F_{1g} \oplus 3A_{2u} \oplus 3E_u \oplus 3F_{2u}$	
Acoustic	F_{1u}	
Raman	$A_{1g} \oplus E_g \oplus 3F_{2g}$	
Infrared	$6F_{1u}$	
Inactive	$F_{1g} \oplus 2A_{2u} \oplus 2E_u \oplus 2F_{2u}$	

was performed by fitting the data to a superposition of Lorentzian bands. The best-fit values for the peak position are reported in Table 2.

The Raman spectrum of $Li_{4/3}Ti_{5/3}O_4$ (Fig. 4) displays a strong high-wavenumber band at 671 cm^{-1} (A_{1g}) with two shoulders at 640 and 747 cm^{-1}. Two bands with medium strength are located at 232 (F_{2g}) and 430 cm^{-1} (E_g), while weaker bands appear at 271 and 347 cm^{-1} (F_{2g}). These RS features are in good agreement with those reported by Liu et al. [13]. The authors have recorded phonon peaks centred at 239, 274, 367, 427 and 675 cm^{-1}. Studies of the RS spectrum of TiO_2 (anatase lattice) in the low-wavenumber region ruled out the existence of bands located at 101, 143, 233, 400 and 515 cm^{-1} which are not observed in the spectrum of the HEBM-$Li_{4/3}Ti_{5/3}O_4$. Similar to other oxide spinels, the interatomic interaction Ti–O dominates the other interatomic interactions, as octahedral bonding (Ti–O, ionic) is stronger than tetrahedral bonding (Li–O, covalent). This indicates that with intercalation of Li to the $LiTi_2O_4$-phase, some of the ionic bonding convert to covalent bonding and hence it shows insulating property. As reported before [6], the white color of $Li_{4/3}Ti_{5/3}O_4$ is an indication of its electronic insulating property. The substitution of Li for Ti in $LiTi_2O_4$ to give $Li_{4/3}Ti_{5/3}O_4$ causes no structural distortion but only a small change in the cubic parameter reflecting the similarity between the ionic radii of Ti^{4+} (0.75 Å, octahedral) and Li^+ (0.73 Å, tetrahedral). The general trend of the RS spectrum of $Li_4Mn_5O_{12}$, which displays resemblance with that of λ-$LiMn_2O_4$, is the frequency shift of the $F_{2g}^{(1)}$ and A_{1g} mode. These two components are recorded at 653 and 634 cm^{-1} (Fig. 4).

As the series of the lithium spinel-type oxides $Li_{1+z}Me_{2-z}O_4$ (Me = Ti, Mn), or $(Li)_{tetr}[Li_zMn_{2-z}]_{oct}O_4$ in spinel notation, contains Li ions in vacant 16d octahedral sites, we can expect a slight tetragonal distortion. The net effect could be a breakdown of the translation symmetry because of the random distribution of the metal ions on the octahedral sites; consequently, a common feature of these RS spectra is the presence of some bands in addition to the Raman-active modes vibrations allowed by the space group theory for an ideal spinel structure. It should also be noted that the emergence of some IR-active F_{1u} modes in the first-order RS spectra was explained by the same

Table 2
Vibrational mode frequencies (cm^{-1}) and assignment of $Li_4Ti_5O_{12}$ and $Li_4Mn_5O_{12}$ spinels

$Li_4Ti_5O_{12}$		$Li_4Mn_5O_{12}$		Assignment
Raman	Infrared	Raman	Infrared	
232		304		F_{2u}
	243		227	F_{2u}
271	272	376	288	F_{2g}
347		434		E_g
	358		370	F_{1u}
	417			F_{1u}
430		491		F_{2g}
	455		465	F_{1u}
	504		518	F_{1u}
640		600		F_{2g}
	592		612	F_{1u}
	650		645	F_{1u}
671		634		A_{1g}
747		653	794	–

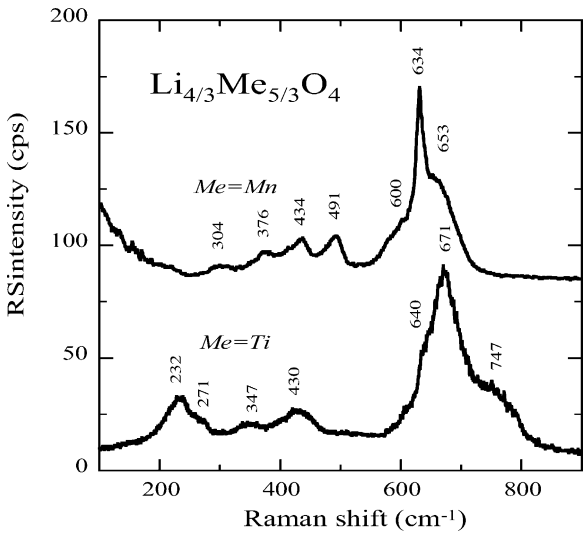

Fig. 4. Raman scattering spectra of $Li_{4/3}Ti_{5/3}O_4$ and $Li_{4/3}Mn_{5/3}O_4$ spinels.

lowering in the symmetry caused by the disordering in the cation sublattice [19,20]. Comparing the RS features with those of λ-$LiMn_2O_4$, the increasing stretching frequency is attributed to the shortness of the Mn–O bonds in $Li_{1.33}Mn_{1.67}O_4$. Due to the presence of the Li atoms in octahedral holes, the frequency of the A_{1g} stretching mode is influenced by bonding and repulsion effects of the tetrahedrally coordinated metal ions [21]. Furthermore, this would be consistent with the fact that the $Li_{1.33}Mn_{1.67}O_4$ spectral features in the low-frequency domain of the RS spectrum are not markedly different from those of $LiMn_2O_4$ where, of course, a significant increase of the peak located at 300 cm^{-1} occurs. It was speculated that this Raman band is partly related to the stretching vibration of Li ions in octahedral coordination [22]. As this peak grows upon lithium occupancy in 16d sites, it is also partly associated with the presence of Mn^{IV}–O bonding.

3.3. Electrochemical features

The electrochemical features of the HEBM-prepared $Li_4Ti_5O_{12}$ powders were tested in lithium cell using a gel–polymer electrolyte. Fig. 5a shows the discharge–charge profile obtained with a Li//$Li_4Ti_5O_{12}$ cell between 1.2 and 2.5 V. The initial OCV was 2.89 V. During discharge, the evolution of the equilibrium potential drops quickly to 1.54 V and displays the characteristic two-phase behavior for the spinel $Li_{1.33}Ti_{1.67}O_4$ electrode.

The initial capacity of 164 mAh/g seems to correlate reasonably well with insertion of one Li per O_4 formula unit. Upon intercalation (discharge) the phase transition process from spinel- to rock-salt-type phase $Li_{1.33+x}Ti_{1.67}O_4 \rightarrow Li_{2.33}Ti_{1.67}O_4$ ($Li_4Ti_5O_{12} \rightarrow Li_7Ti_5O_{12}$) starts to dominate the electrode kinetics. The OCV curve versus x (Li) is constant in the Li composition range $0.05 \leq x \leq 0.85$. This curve slightly decreases from 0.9 before to drop sharply at $x \approx 0.95$. A two-phase electrochemical reaction occurs as a flat voltage response; in this reaction, a distinct change in voltage is evident as one phase becomes depleted, thus providing an end-of-charge indicator [23]. These features are evident for $Li_4Ti_5O_{12}$ in Fig. 5a.

Fig. 5b displays the electrochemical profiles of the discharge–charge curves at C/12 rate for a Li//$Li_4Ti_5O_{12}$ cell using SPE:copolymer gel electrolyte. The first coulombic efficiency (ICE) was 96%. The cell delivered a gravimetric capacity of 157 mAh/g, which may be compared to the theoretical capacity of about 175 mAh/g; the small hysteresis detected between charge and discharge curve ($\Delta V \approx 0.1$ V) is likely ohmic in nature. As reported earlier [3,4], the good cyclability of $Li_4Ti_5O_{12}$ spinel is observed because the cubic unit cell expands and contracts by less than 1% within controlled compositional limits ($0.00 \leq x \leq 0.95$). Considering the structural model proposed by Ohzuku et al., the reduction process $Ti^{4+} \rightarrow Ti^{3+}$ is associated with the occupation of all 16c octahedral site by Li ions [6]. Accordingly, $Li_4Ti_5O_{12}$ is a site-limited insertion compound

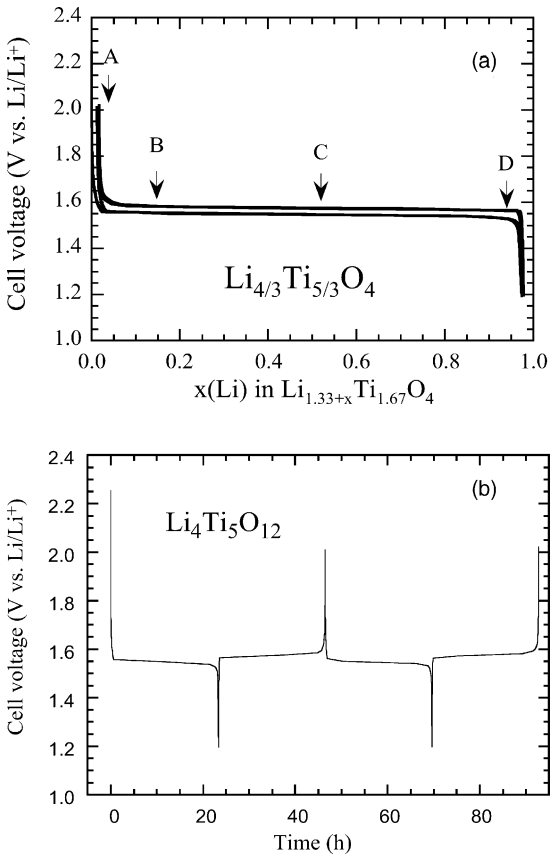

Fig. 5. (a) The discharge–charge curves of Li//$Li_{1.33+x}Ti_{1.67}O_4$ cell as a function of the lithium content. Arrows indicate the composition for Raman analysis. (b) Electrochemical profiles of the discharge–charge curves at C/12 rate for a Li//$Li_4Ti_5O_{12}$ cell using SPE:copolymer gel electrolyte.

due to the final product $[Li_2]^{16c}[Li_{0.33}Ti_{1.67}]^{16d}O_4$ in spinel notation.

Fig. 6 displays the discharge–charge curve of Li//$Li_4Mn_5O_4$ cell. As reported previously [24,25], the $[Me^{IV}]O_6$ framework of $Li[Li_{1/3}Mn_{5/3}]O_4$ spinel is an attractive host structure for lithium insertion–extraction reactions because it

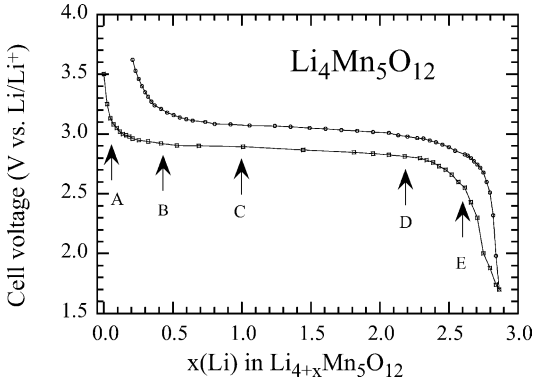

Fig. 6. Electrochemical profiles of the discharge–charge curves as a function of the lithium content in $Li_{1.33+x}Mn_{1.67}O_4$ cell. Arrows indicate the composition for Raman analysis.

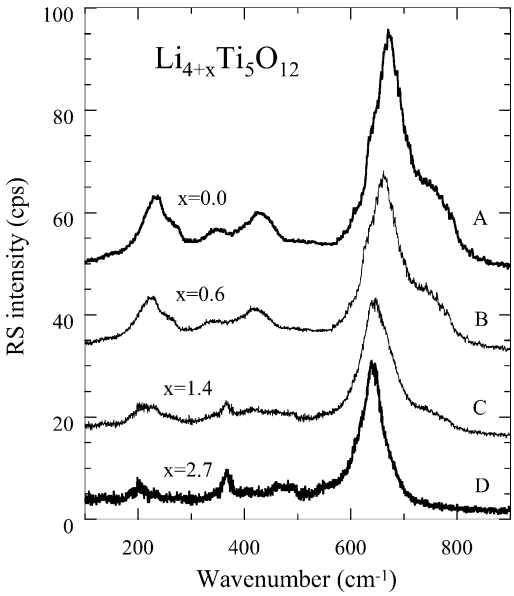

Fig. 7. The Raman spectra of $Li_{1.33+x}Mn_{1.66}O_4$ electrode materials at different amounts of lithium insertion. The final product shows the tetragonal feature.

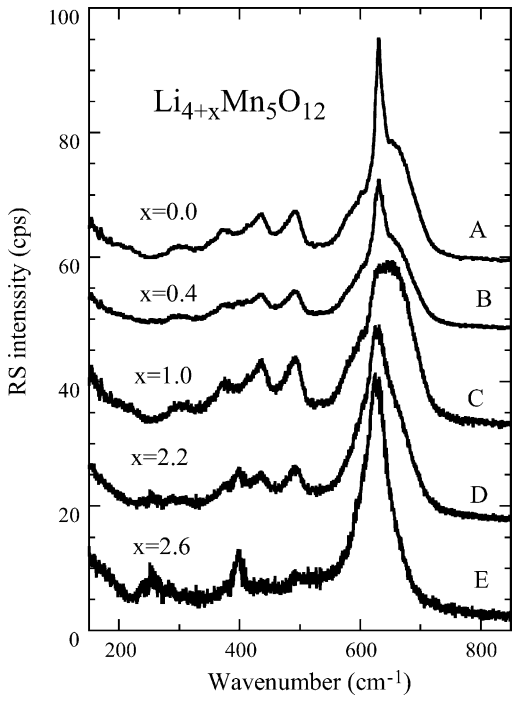

Fig. 8. The Raman spectra of $Li_{1.33+x}Mn_{1.66}O_4$ electrode materials versus lithium insertion. The final product shows the tetragonal feature.

provides a three-dimensional network of face-sharing tetrahedra and octahedra for lithium-ion diffusion. $Li_{4/3}Mn_{5/3}O_4$ has a capacity of 163 mAh/g in the potential range 3.5–1.5 V.

3.4. Phase evolution upon lithium insertion

Fig. 7 (curves A–D) displays the RS spectrum of electrochemically lithiated $Li_{4+x}Ti_5O_{12}$ spinel recorded on materials taken from a cell discharged from 2.0 to 1.2 V. The evolution of the RS spectra shows clearly the structural changes that occurred in $Li_{4/3}Ti_{5/3}O_4$ upon Li insertion. The fully lithiated product ($Li_7Ti_5O_{12}$) displays a tetragonal structure with $I4_1/amd$ (D^{19}_{4h}) space group, which induces three typical low-wavenumber Raman bands located at 200, 360 and 465 cm^{-1}. The Ti–O stretching mode displays a red shift due to the reduction of Ti ions, a consequence of the lithium insertion in octahedral 16c empty sites. The high-frequency band appears at 642 cm^{-1} that corresponds to a shift of 30 cm^{-1} from the cubic lattice. As the discharge mechanism occurs with the appearance of a plateau at 1.55 V (two-phase region), the RS spectrum (curve C) appears as the superposition of two spectra of the end-members, i.e. $Li_4Ti_5O_{12}$ and $Li_7Ti_5O_{12}$. For $Li_7Ti_5O_{12}$, factor group theory predicts $2A_{1g} + 4E_g + B_{1g} + 3B_{2g}$ Raman-active modes. Surprisingly, there are only six bands observed in the RS spectrum of $Li_7Ti_5O_{12}$. The lack of additional bands could be due to the weak Raman-activity of these expected additional bands. Furthermore, the whole spectral features $Li_7Ti_5O_{12}$ are consistent with the tetragonal $I4_1/amd$ space group.

Fig. 8 (curves A–E) shows the RS spectrum of electrochemically lithiated $Li_{6.5}Mn_5O_{12}$ spinel recorded on material taken from a cell discharged at 2.5 V. The RS spectrum of $Li_{6.5}Mn_5O_{12}$ shows clearly the structural change that occurred in $Li_{4/3}Mn_{5/3}O_4$ upon Li insertion from cubic (O^7_h) to tetragonal (D^{19}_{4h}) structure. This structural modification induces three typical low-wavenumber RS bands located at 255, 282 and 397 cm^{-1}. The high-frequency band appears at 628 cm^{-1} with a shoulder at 592 cm^{-1}. Similarly to $Li_7Ti_5O_{12}$, spectral features $Li_{6.5}Mn_5O_{12}$ are consistent with the tetragonal $I4_1/amd$ space group. A tetragonal distortion is expected to occur with the Li insertion in $Li_{4/3}Mn_{5/3}O_4$ because of appearance of the Mn^{3+} JT ions at the end of the discharge. The net effect is a lowering in the crystal symmetry from cubic *Fd*3*m* to tetragonal $I4_1/amd$.

4. Conclusion

Well-crystallized $Li_{4/3}Me_{5/3}O_4$ powders with Me = Ti and Mn have been synthesized by high-energy ball milling and 'chimie douce', respectively. Powders with submicron-sized grains were obtained. The structure of $Li_{4/3}Me_{5/3}O_4$ particles was found to be cubic spinel (*Fd*3*m* space group) with unit cell parameter $a = 8.365(2)$ Å and $a = 8.161(1)$ Å for Ti and Mn compounds, respectively. We confirmed that Li ions occupy both the tetrahedral 8a and octahedral 16d sites using Raman spectroscopy. Vibrational features are in good concordance with the factor group analysis (O^7_h symmetry). The zero-strain insertion material $Li_{4/3}Ti_{5/3}O_4$ delivers 150 mAh/g while $Li_{4/3}Mn_{5/3}O_4$ inserts 2.8 Li per mole of oxide leading to a specific capacity of 158 mAh/g. The phase evolution of $Li_{4+x}Ti_5O_{12}$ and

$Li_{4+x}Mn_5O_{12}$ electrochemically lithiated has been studied by Raman spectroscopy. The net effect is a lowering in the crystal symmetry from cubic $Fd3m$ to tetragonal $I4_1/amd$.

Acknowledgements

The author would like to thank Mr. Michel Lemal for his careful work in performing the XRD measurements.

References

[1] M.R. Harrison, P.P. Edwards, J.B. Goodenough, Philos. Mag. B 52 (1985) 679.
[2] C. Julien, NATO Sci. Ser. 3–85 (2000) 1.
[3] K. Zaghib, M. Armand, M. Gauthier, J. Electrochem. Soc. 145 (1998) 3135.
[4] K. Zaghib, M. Simoneau, M. Armand, M. Gauthier, J. Power Sources 81–82 (1999) 300.
[5] K.M. Colbow, J.R. Dahn, R.R. Haering, J. Power Sources 26 (1989) 397.
[6] E. Rossen, J.N. Reimers, J.R. Dahn, Solid State Ionics 62 (1993) 53.
[7] T. Ohzuku, A. Ueda, Solid State Ionics 69 (1994) 201.
[8] T. Ohzuku, A. Ueda, N. Yamamoto, J. Electrochem. Soc. 142 (1995) 1431.
[9] S. Bach, J.P. Pereira-Ramos, N. Baffier, J. Mater. Chem. 8 (1998) 251.
[10] S. Bach, J.P. Pereira-Ramos, N. Baffier, J. Power Sources 81–82 (1999) 273.
[11] A.N. Jansen, A.J. Kahaian, K.D. Kepler, P.A. Nelson, K. Amine, D.W. Dees, et al., J. Power Sources 81–82 (1999) 902.
[12] S. Scharner, W. Weppner, P. Schmid-Beurmann, J. Electrochem. Soc. 146 (1999) 857.
[13] D.Z. Liu, W. Haynes, M. Kurmoo, M. Dalton, C. Chen, Physica C 235–240 (1994) 1203.
[14] M.M. Sinha, H.C. Gupta, Phys. Status Solidi B 221 (2000) 689.
[15] C.M. Julien, M. Massot, J. Phys. Cond. Matter 15 (2003) 3151.
[16] C. Julien, S. Ziolkiewicz, M. Lemal, M. Massot, J. Mater. Chem. 11 (2001) 1837.
[17] W.B. White, B.A. De Angelis, Spectrochim. Acta 23A (1967) 985.
[18] G.C. Allen, M. Paul, Appl. Spectrosc. 49 (1995) 451.
[19] P.P. Posini, R. Mancini, L. Petrucci, V. Contini, P. Villano, Solid State Ionics 144 (2001) 185.
[20] R. Stoyanova, M. Gorova, E. Zhecheva, J. Phys. Chem. Solids 61 (2000) 615.
[21] C. Julien, Solid State Ionics 136–137 (2000) 887.
[22] C. Julien, NATO Sci. Ser. 3–85 (2000) 309.
[23] P. Endres, B. Fuchs, S. Kemmler-Sack, K. Brandt, G. Faust-Becker, H.W. Praas, Solid State Ionics 89 (1996) 221.
[24] M.M. Thackeray, Prog. Solid St. Chem. 25 (1997) 1.
[25] T. Takada, H. Hayakawa, E. Akiba, F. Izumi, B.C. Chakoumakos, J. Power Sources 68 (1997) 613.